

Polarization and angular dependent transmissions on transferred nanomembrane Fano filters

Li Chen¹, Zexuan Qiang^{1,2}, Hongjun Yang¹, Huiqing Pang³, Zhenqiang Ma³, and Weidong Zhou^{1*}

¹Department of Electrical Engineering, NanoFAB Center, University of Texas at Arlington, Texas 76019, USA.

²School of Physics and Optoelectronics Technology, Fujian Normal University, Fuzhou, 35007, P. R. China

³Department of Electrical and Computer Engineering, University of Wisconsin-Madison, Wisconsin 53706, USA

*w:zhou@uta.edu

Abstract: We report angular and polarization dependent transmission properties of Fano resonance optical filters with transferred silicon nanomembrane on glass substrate. The transmission spectra of the filters can have either weak or strong polarization and angular dependence, depending on properties of individual Fano resonance modal dispersion. Measurement results agree very well with simulations based on a rigorous coupled-wave analysis for the transmission spectra, on planewave expansion wave-vector technique for the dispersion property analysis, and on a three-dimensional finite-difference time-domain technique for the propagating modal study. These results will provide importance guidance for the design of a new class of ultra-compact surface-normal frequency selective components with preferred polarization and angular properties. These components are highly desirable for silicon photonic integration.

©2009 Optical Society of America

OCIS codes: (050.2770) Gratings; (060.1810) Couplers, switches, and multiplexers; (230.0230) Optical devices; (250.5300) Photonic integrated circuits; (130.3130) Integrated optics materials; (230.7390) Waveguides; (130.0130) Integrated Optics; (999.9999) Photonic crystals.

References and links

1. S. Fan, and J. D. Joannopoulos, "Analysis of guided resonances in photonic crystal slabs," *Phys. Rev. B* **65**(23), 235112 (2002).
2. R. Magnusson, and S. S. Wang, "New principle for optical filters," *Appl. Phys. Lett.* **61**(9), 1022 (1992).
3. C. Lin, Z. Lu, S. Shi, G. Jin, and D. W. Prather, "Experimentally demonstrated filters based on guided resonance of photonic-crystal films," *Appl. Phys. Lett.* **87**(9), 091102 (2005).
4. A. Rosenberg, M. Carter, J. Casey, M. Kim, R. Holm, R. Henry, C. Eddy, V. Shamamian, K. Bussmann, S. Shi, and D. W. Prather, "Guided resonances in asymmetrical GaN photonic crystal slabs observed in the visible spectrum," *Opt. Express* **13**(17), 6564–6571 (2005).
5. W. Suh, and S. Fan, "All-pass transmission or flattop reflection filters using a single photonic crystal slab," *Appl. Phys. Lett.* **84**(24), 4905 (2004).
6. S. Boutami, B. B. Bakir, H. Hattori, X. Letartre, J.-L. Leclercq, P. Rojo-Rome, M. Garrigues, C. Seassal, and P. Viktorovitch, "Broadband and compact 2-D photonic crystal reflectors with controllable polarization dependence," *IEEE Photon. Technol. Lett.* **18**(7), 835–837 (2006).
7. A. R. Cowan, and J. F. Young, "Optical bistability involving photonic crystal microcavities and Fano line shapes," *Phys. Rev. E Stat. Nonlin. Soft Matter Phys.* **68**(4), 046606 (2003).
8. X. Yang, C. Husko, C. W. Wong, M. Yu, and D.-L. Kwong, "Observation of femtojoule optical bistability involving Fano resonances in high-Q/V_{sub m} silicon photonic crystal nanocavities," *Appl. Phys. Lett.* **91**(5), 051113 (2007).
9. S. A. Scott, and M. G. Lagally, "Elastically strain-sharing nanomembranes: flexible and transferable strained silicon and silicon-germanium alloys," *J. Phys. D Appl. Phys.* **40**(4), R75–R92 (2007).
10. H. C. Yuan, Z. Ma, M. M. Roberts, D. E. Savage, and M. G. Lagally, "High-speed strained-single-crystal-silicon thin-film transistors on flexible polymers," *J. Appl. Phys.* **100**(1), 013708 (2006).
11. J. A. Rogers, Z. Bao, K. Baldwin, A. Dodabalapur, B. Crone, V. R. Raju, V. Kuck, H. Katz, K. Amundson, J. Ewing, and P. Drzaic, "Paper-like electronic displays: large-area rubber-stamped plastic sheets of electronics and microencapsulated electrophoretic inks," *Proc. Natl. Acad. Sci. U.S.A.* **98**(9), 4835–4840 (2001).

12. H. Yuan, G. Celler, and Z. Ma, "7.8-GHz flexible thin-film transistors on a low-temperature plastic substrate," *J. Appl. Phys.* **102**(3), 034501 (2007).
13. H. Yang, Z. Qiang, H. Pang, Z. Ma, and W. D. Zhou, "Surface-Normal Fano Filters Based on Transferred Silicon Nanomembranes on Glass Substrates," *Electron. Lett.* **44**(14), 858–859 (2008).
14. Z. Qiang, H. Yang, L. Chen, H. Pang, Z. Ma, and W. Zhou, "Fano filters based on transferred silicon nanomembranes on plastic substrates," *Appl. Phys. Lett.* **93**(6), 061106 (2008).
15. S. Peng, and G. Morris, "Resonant scattering from two-dimensional gratings," *J. Opt. Soc. Am. A* **13**(5), 993–1005 (1996).
16. G. Niederer, W. Nakagawa, H. Herzig, and H. Thiele, "Design and characterization of a tunable polarization-independent resonant grating filter," *Opt. Express* **13**(6), 2196–2200 (2005).
17. D. Crouse, and P. Keshavareddy, "Polarization independent enhanced optical transmission in one-dimensional gratings and device applications," *Opt. Express* **15**(4), 1415–1427 (2007).
18. V. Lousse, W. Suh, O. Kilic, S. Kim, O. Solgaard, and S. Fan, "Angular and polarization properties of a photonic crystal slab mirror," *Opt. Express* **12**(8), 1575–1582 (2004).
19. J. Song, R. Proietti Zaccaria, M. B. Yu, and X. W. Sun, "Tunable Fano resonance in photonic crystal slabs," *Opt. Express* **14**(19), 8812–8826 (2006).
20. Z. Qiang, W. D. Zhou, M. Lu, and G. J. Brown, "Fano Resonance Enhanced Infrared Absorption for Infrared Photodetectors," *Proc. SPIE* **6901**, 69010F (2008).
21. H.-C. Yuan, G. K. Celler, and Z. Ma, "7.8-GHz flexible thin-film transistors on a low-temperature plastic substrate," *J. Appl. Phys.* **102**(3), 034501 (2007).
22. M. G. Moharam, and T. K. Gaylord, "Rigorous coupled-wave analysis of planar-grating diffraction," *J. Opt. Soc. Am.* **71**(7), 811–818 (1981).
23. K. C. Johnson, "Coupled scalar wave diffraction theory," *Appl. Phys., A Mater. Sci. Process.* **24**, 249–260 (1981).
24. E. Drouard, H. Hattori, C. Grillet, A. Kazmierczak, X. Letartre, P. Rojo-Romeo, and P. Viktorovitch, "Directional channel-drop filter based on a slow Bloch mode photonic crystal waveguide section," *Opt. Express* **13**(8), 3037–3048 (2005).
25. W. Zhou, Z. Qiang, and L. Chen, "Photonic crystal defect mode cavity modelling: a phenomenological dimensional reduction approach," *J. Phys. D.* **40**(9), 2615–2623 (2007).

1. Introduction

Surface-normal ultra-compact optical filters are of great importance in optical fiber communications, optical sensors, and millimeter-wave communication systems. Traditional thin-film based filters, operating in the infrared regime for dense wavelength division multiplexing (DWDM) applications, usually require hundreds of or more individual layers, with stringent thickness tolerances for each layer and are thus very difficult to satisfy missions of nanophotonics. Photonic crystal slabs (PCS) are one of the most promising artificial platforms with in-plane periodic modulation of dielectric constant on a wavelength scale. The out-of-the-plane optical mode coupling is feasible with the Fano or guided resonance effect [1,2], where these in-plane guided resonances above the lightline are also strongly coupled to out-of-the-plane radiation modes due to phase matching provided by the periodic lattice structure. Therefore, the guided resonances can provide an efficient way to channel light from within the slab to the external environment, and vice versa [1]. In recent years, devices based on Fano resonance like narrowband filters [2–4] broadband reflectors [5,6], and Fano resonances for non-linear optical bistabilities [7,8] have all been proposed and reported.

Recently, crystalline semiconductor nanomembranes (NMs) have attracted great attention since they are transferable, stackable, bondable and manufacturable, offering unprecedented opportunities for unique and novel electronic and photonic devices for vertically stacked high density photonic/electronic integration. High-quality single crystalline silicon NMs (SiNM) have been transferred onto various foreign substrates, such as glass, plastics, etc., using low temperature transfer processes, developed by various groups [9–12]. Recently, we have successfully demonstrated Fano filters based on patterned silicon nanomembranes (SiNMs) transferred onto transparent low index glass and flexible polymer substrates [13,14].

In this paper, we report the detailed analysis on the polarization and angle dependent transmission properties on Si Fano filters transferred onto glass substrate. Fano resonances can be manipulated by varying the phase matching conditions between the coupled guided resonant modes and radiation modes, through the control of incident beam direction and polarization. Angular- and polarization- properties have been reported for one-dimensional

diffraction grating structures [15–17] and for two-dimensional Fano filters on suspended symmetric photonic crystal slabs [18,19]. The Fano filters reported here, fabricated with transferred SiNMs on low index glass substrates, are expected to have different polarization- and angular- dependent transmission properties due to the asymmetric vertical confinement. In what follows, we first briefly describe the design, fabrication and characteristics of Fano filters on glass substrates, followed by detailed analysis on the measured and simulated angular- and polarization- dependent transmission properties. A conclusion is given in the end.

2. Fano filters with patterned Si nanomembranes transferred on glass substrates

Photonic crystal (PC) structures were first designed with a three-dimensional finite-difference time domain (3D FDTD) technique by using periodic boundary condition (PBC) and perfectly matched layer (PML) in the four lateral and in the vertical directions, respectively [1,20]. The PC was fabricated with a target Fano filter wavelength of 1550 nm, on silicon-on-insulator (SOI) wafers, using e-beam lithography and plasma dry-etching processes [14]. Shown in Fig. 1(a) and Fig. 1(b) are the schematic and the scanning electron micrographs (SEMs) of the patterned square lattice PC SOI structures, respectively, where the periodicity (a) and air hole radius (r) in this structure are 600 nm and 114 nm, respectively. The thickness of the template Si layer is 250 nm. As shown schematically in Fig. 1(c), the patterned PC SOI structures were subsequently transferred onto a glass substrate, using on a modified wet transfer process [13,14,21]. An SEM image of a transferred large-area patterned SiNM is shown in Fig. 1(d), with the inset showing a micrograph of a 5mm x5mm patterned SiNM piece (center golden colored piece) transferred onto a 1"x1" glass slide.

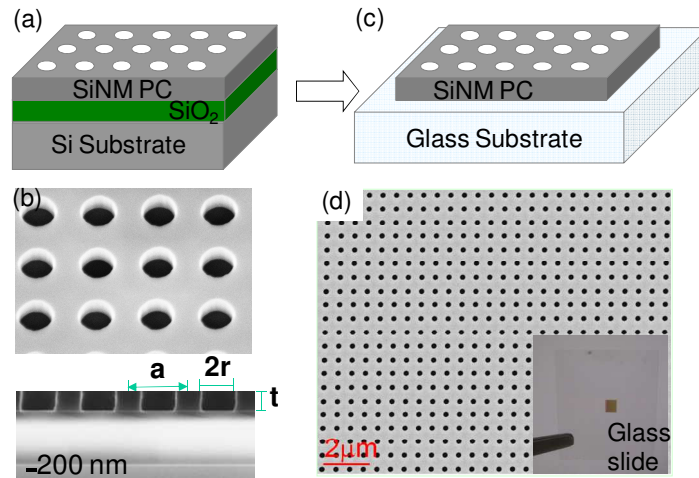


Fig. 1. (a) Schematic and (b) scanning electron micrographs (SEMs) of photonic crystal (PC) patterned structure on the SOI wafer; (c) Schematic of PC patterned SiNM transferred on a glass substrate; and (d) SEM top view of a transferred SiNM on glass, with inset showing the micrograph of completely transferred patterned SiNM piece on a glass slide substrate.

The measured Fano filter transmission characteristics were shown in Fig. 2(a). The experiment was conducted with an unpolarized and focused broadband QTH (quartz tungsten halogen) lamp source. The focused beam size is $\sim 150 \mu\text{m}$ in diameter, much smaller than the 2-5 mm patterned device area, but sufficiently larger than the lattice constant a of $0.6 \mu\text{m}$. The measured transmission spectrum of SiNM was obtained by normalizing the measured transmission spectral intensity data for Fano filters to the data for the glass substrate (reference). At certain spectral locations, close to 100% transmission was obtained. A

dominant dip was observed at the target wavelength of 1547 nm (denoted as λ_1) and other two dips were observed at around 1417 nm (λ_2) and 1393 nm (λ_3), respectively.

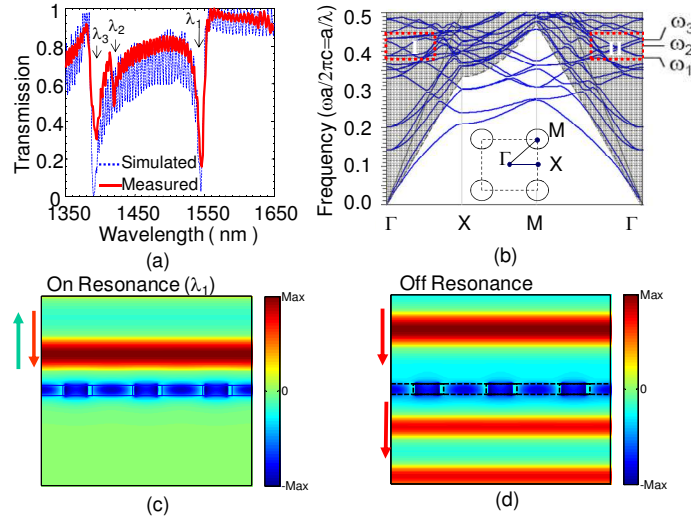


Fig. 2. (a) Measured and simulated surface normal transmission spectra for the fabricated patterned SiNM Fano filters on glass substrates; (b) Simulated dispersion plot for Fano filters on glass substrates, where $r/a = 0.19$, $t/a = 0.25/0.6 \sim 0.417$. The refractive indices of silicon and glass are 3.48 and 1.5, respectively. Note the surface-normal transmission dips/peaks at all three wavelength points (λ_1 , λ_2 , λ_3) agree well with the dispersion plot ω_1 , ω_2 , ω_3 at Γ point. (c) and (d) The simulated snapshots of electrical field intensity profiles for on-resonance wavelength (λ_1) and off-resonances, respectively.

Rigorous coupled-wave analysis (RCWA) [22,23] was carried out to find out the target resonance wavelength at 1547 nm for the square lattice silicon PCS on the glass substrate. The dotted blue curve shown in Fig. 2(a) is the simulated transmission response of such a structure under surface-normal condition, which agrees very well with the measured transmission spectra. The spectral bandwidth and quality factor of the filter resonance can be further optimized to have either very high Q ($>1,000$), or very low Q (broadband), by design optimization, control of modal symmetry, choice of lattice configurations, and choice of lattice parameters. The choice in the fill factor, i.e., r/a ratio, can significantly alter the device characteristics. Typically, small fill factor can lead to high- Q narrow band filters, and larger fill factor can lead to broadband filters/reflectors [1].

It is worth mentioning that the measured transmission spectra agree very well with the original design, with slight shift in the resonance locations. Care was taken to ensure that the fabricated device has the same lattice parameters (air hole radius r and lattice constant a). In order to fit the measured resonance locations, SiNM thickness was adjusted from the design value of 260 nm to the fit value of 250 nm, within the thickness variation specifications from Soitec wafer datasheet. Excellent agreement was obtained for both simulation and experiment. For all the simulations carried out in this work. All these structural parameters kept the same for the same device.

Notice that strong oscillations in the simulated transmission spectra are due to the Fabry-Perot interferences caused by the truncated finite thickness of glass substrate during simulation. Comparing simulation and experiment, the differences in the quality factor and thus the Bloch mode lifetime [24] are small ($<10\%$). However, the transmission contrast ratio seems to be large (4dB difference for spectra shown in Fig. 2(a)). This could be due to our measurement error, as well as fabrication imperfections.

Additionally, these three resonance modes can be correlated to the bandedge mode at the zone center (Γ point) for the surface-normal incident beams. Shown in Fig. 2(b) is the

simulated dispersion plot for the square lattice structure under testing, based on a planewave expansion (PWE) technique. All the three dips obtained in the transmission spectra (λ_1 , λ_2 , and λ_3) agree well with the three modes obtained from the simulated dispersion plot, labeled as ω_1 , ω_2 , and ω_3 , respectively.

The resonance modes were further verified with three dimensional finite difference time domain (3D FDTD) simulations. The snapshots of field propagation for both on- and off-resonance modes are shown in Fig. 2(c) and 2(d), respectively. Note that, for the on-resonance mode (λ_1), the surface-normal incident light is bounced back from the patterned SiNM structure due to the coherence (in-phase) reflection, which leads to the dip in the transmission spectra. On the other hand, light at other spectra locations (off-resonance) can pass through the patterned SiNM Fano filter with its maximum transmission efficiency.

3. Angular- and polarization-dependent properties of the Fano filter

Detailed investigations were then carried out on the angular- and polarization-dependent transmission characteristics for this type of Fano filters on glass substrates. As shown in Fig. 3, the light incident direction is defined by two polar angles, the colatitude angle θ (angle from the surface-normal direction) and the azimuth angle ϕ (angle from the positive x -axis to the orthogonal projection of the incident beam in the x - y plane).

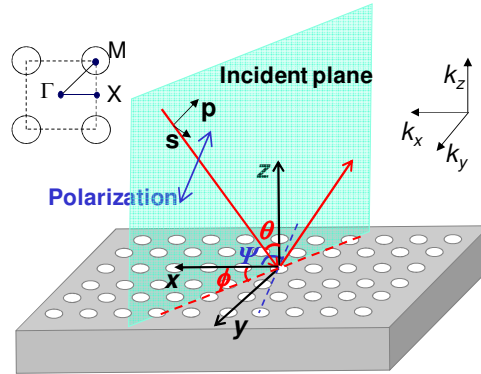


Fig. 3. Angle and polarization definition for incident light beam onto patterned SiNM Fano filters. The PC lattice and Brillouin zone symmetric points (Γ , X and M) in the k -space are also shown in the inset.

The incident polarization (E-vector) angle Ψ is defined as the angle from the positive x -axis to the projection of polarization direction in the x - y plane. Following a conventional definition, typical s- or p-polarizations are defined as the beam with E-vector perpendicular or parallel to the incident plane formed by the incident light and reflected light, i.e., $\Psi = \phi$ for p- (TM-like) polarization and $\Psi = \phi + 90^\circ$ for s- (TE-like) polarization. Also shown in Fig. 3 are the conventional definition of wavevector directions and the corresponding Brillouin zone in k -space with high symmetric points defined with Γ , X and M , respectively. Due to the high symmetric properties of the square lattice in the device, we only considered three special cases in this study: (i) Surface-normal without and with polarizations ($\theta = 0^\circ$, varying ϕ , at Γ point in k -space); (ii) With incident beam plane parallel to x - z plane ($\phi = 0^\circ$, varying θ , along Γ - X direction in k -space); and (iii) With incident beam plane 45 degree off x - z plane ($\phi = 45^\circ$, varying θ , along Γ - M direction in k -space).

3.1. Case I: Surface-normal incidence without and with polarizations

We first investigate the transmission properties for surface-normal incident conditions, with $\theta = 0^\circ$. The measurement results are shown in Fig. 4, for different angles ϕ , as defined in Fig. 3.

The polarization of incident beam is controlled by inserting a linear polarizer between the broadband light source and the objective lens in front of the test sample.

The results shown in Fig. 4(a) and Fig. 4(b) are for two cases without polarizer and with polarizer, respectively. Similar to the work reported earlier on free-standing filters [18] and on flexible plastic PET substrate [14], very little spectral shifts were observed on the transmission spectra for all the three Fano resonant modes. The angle (ϕ) and polarization (Ψ) independent transmission characteristics at $\theta = 0^\circ$ are the results of the high symmetry of the circular-air-hole square lattice. Again the small variations on the measured transmission efficiencies could be related to the measurement error associated with fabrication imperfection of the lattice during the SiNM transfer processes.

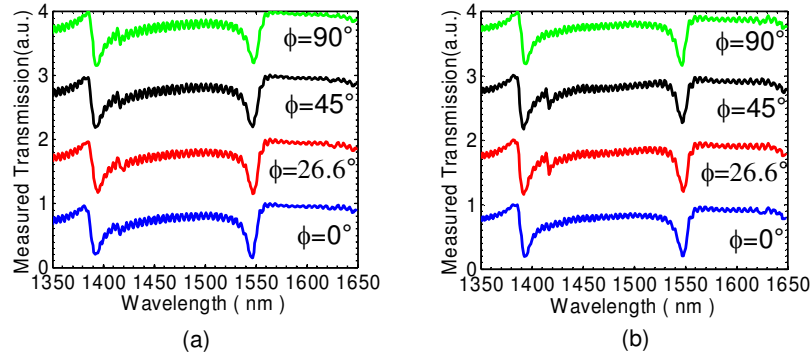


Fig. 4. Measured surface-normal transmission spectra at different angles ϕ for the incident beam either (a) without polarizer; or (b) with polarizer fixed at $\psi = 0$.

3.2. Case II: With incident beam plane in parallel with x - z plane (Γ - X direction)

In this case, the incident beam is restricted to be within the plane in parallel with the x - z plane, i.e., kept at $\phi = 0^\circ$. This corresponds to the Γ - X direction in the k -space. The measured transmission spectra intensity contour plots for different incident angles (θ) are shown in Fig. 5(a) and 5(b) for the p - and the s -polarized incident beams, respectively. The simulated transmission spectra, based on the RCWA technique, are shown in Fig. 5(c) and 5(d), with the simulation parameters and test conditions matching with the measurement results shown in Fig. 5(a) and 5(b), respectively. Notice that the plots for the simulated spectra are rotated in order to have a better visual comparison between the experimental results and the simulation results.

When the incident beam is p -polarized (TM-like), i.e., the electrical vector direction lies in the plane that is in parallel with the incident beam plane, the dominant Fano resonant mode ($\lambda_1 = 1547$ nm transmission dip at $\theta = 0^\circ$) has very little spectral shift over the range of angles measured (from 0° to 20°). On the other hand, the other two modes show strong angle dependent behavior. The mode at λ_2 shifted towards longer wavelengths, from 1420 nm at $\theta = 0^\circ$ to 1500 nm at $\theta = 20^\circ$, at a constant rate of 4 nm/degree. The mode at λ_3 (1394 nm at $\theta = 0^\circ$) shows very small angle dependence for small incident angles (from 0° to 10°). But it is completely suppressed for larger incident angles ($\theta > 15^\circ$). The simulation results shown in Fig. 5(c) also agree very well with the measurement results shown in Fig. 5(a).

However, for s -polarized (TE-like) incident beam, the dominant Fano resonance mode (λ_1) shifted towards shorter wavelengths (Fig. 5(b, d), from 1547 nm at $\theta = 0^\circ$ to 1448 nm at $\theta = 20^\circ$, at a constant rate of 5 nm/degree. But the mode at the short wavelength (λ_3) has very weak angle dependence, with a small blue-shift less than 10 nm, or 0.5 nm/degree when increasing the incident angle θ from 0° to 20° . Also notice that there is no dip observed at the λ_2 location in this case.

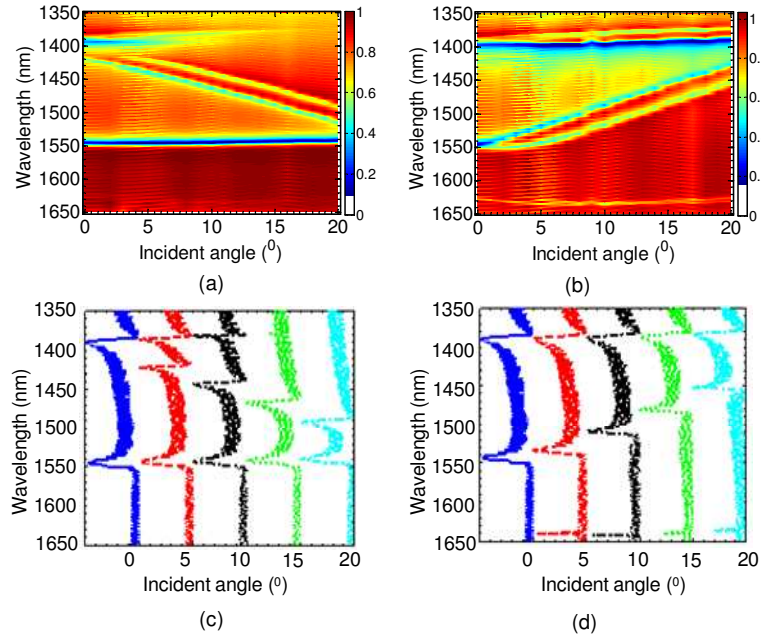


Fig. 5. Measured transmission intensity contour plots under different polarization conditions (a) Γ -X direction with p -polarization light (b) Γ -X direction with s -polarization light; (c, d) Simulated transmission spectra under p - and s -polarizations, respectively.

The polarization dependent behavior for Fano resonances was further investigated with the modal propagation simulation based on a 3D FDTD technique. The simulated snapshots of the propagating electrical fields for the dominant Fano resonance (λ_1) are shown in Fig. 6 for the p - and s -polarized incident beams, with angled incident beam $\theta = 20^\circ$ and $\phi = 0^\circ$. From Fig. 6(a), the guided resonant mode within the patterned SiNM slab region is an even mode (symmetric) with respect to the propagating (z -) direction, similar to the field shown in Fig. 2(c) under the surface-normal incident beam condition. These modes (λ_1) seem to have less angle-dependent transmission properties, most likely related to the relatively unchanged phase-matching conditions for on-resonance, associated with the relatively flat modal dispersion properties. On the other hand, for the s -polarized incident beam, as shown in Fig. 6(c), the guided resonance mode is an odd mode (asymmetric) with respect to the propagating (z -) direction. Changes in the incident angle (θ) may lead to large changes in the spectral location of resonance due to the change in phase matching conditions.

In addition to p - and s -polarizations, incident beams with hybrid polarization ($\Psi = 45^\circ$) was also considered. The measured transmission intensity contour is shown in Fig. 7(a). The dominant Fano resonant mode with $\lambda_1 = 1547$ nm at $\theta = 0^\circ$ splits into two separate degenerate modes for larger incident angles, with one mode remaining at the same spectral location (p -polarization, Fig. 5(a), also confirmed later) and the other shifting towards shorter wavelengths (s -polarization, Fig. 5(b)). This result agrees very well with the data shown in Fig. 5 for both the p - and s -polarized modes. In addition, with the increase of the incident angle, the resonant mode at λ_2 shifts towards longer wavelengths, and the resonant mode at λ_3 remains almost unchanged.

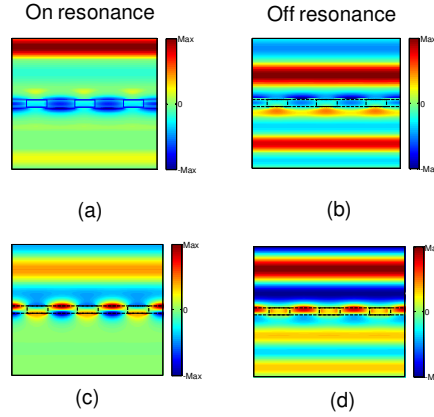


Fig. 6. Snapshots of electric field distributions of Fano filters at large incident angle ($\theta = 20^\circ$ and $\phi = 0^\circ$): (a) p -polarization, on-resonance; (b) p -polarization, off-resonance; (c) s -polarization, on-resonance; and (d) s -polarization, off-resonance.

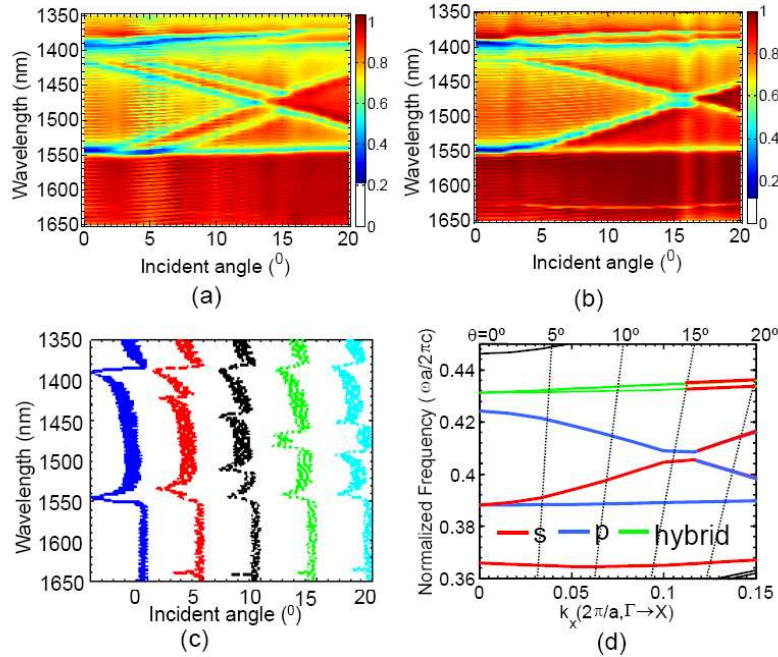


Fig. 7. Measured transmission intensity contour plots for incident beam lies within x - z plane (along Γ - X direction) with (a) hybrid polarization ($\psi = 45^\circ$) and (b) without polarization. (c) Simulated transmission spectra for different incident angles with the same incident beam orientation and polarization shown in (a). (d) Dispersion plot along Γ - X shown the p - and s -polarization states.

It is worth pointing out that such a diagonal polarization light should have both s - and p -polarization components. Therefore, in theory, it is expected that similar transmission results should be generated even from an unpolarized incident beam. This is indeed the case, as shown in Fig. 7(b), which exhibits very similar characteristics as the one shown in Fig. 7(a). The results match very well with the simulated transmission spectra based on the RCWA technique, as shown in Fig. 7(c).

Further analysis was carried out to correlate the measured transmission spectra with the Fano resonant mode based on dispersion plot shown in Fig. 2(b). Following a similar process

reported earlier [14], a correlation was found between the incident angle θ and the wavevector k , with $k_{\Gamma-x} = (\frac{\pi}{\lambda}) \sin \theta$. The corresponding dispersion plot is shown in Fig. 7(d), which is the zoom-in plot of the region I shown in Fig. 2(b). The corresponding p -, s - and hybrid polarized modes are shown with different colors. An excellent agreement between the measurement data and the simulation results has been obtained, which also confirms the earlier analysis on the transmission spectra.

3.3. Case II: With incident beam plane 45 degree off x - z plane (along Γ - M direction)

Finally, we measured the transmission characteristics for the incident beam 45 degree off the x - z plane, i.e. $\phi = 45^\circ$. This is another high symmetry direction, which corresponds to the Γ - M direction in the k -space. The measured transmission intensity contours, along with the simulated transmission spectra, for both the p - and the s -polarized beams, are shown in Fig. 8. Again, the simulation results agree very well with the measured transmission results. For the dominant resonant mode at λ_1 , the transmission spectra shift towards shorter wavelengths for both the p - and the s -polarized beams. For the other mode at λ_2 , shift is only seen with s -polarized beam, differing from the results shown in Fig. 5, where shift is only seen with p -polarized beam. In both cases, the transmission spectra shift towards longer wavelengths. For the mode at λ_3 , it shifts towards shorter wavelengths or longer wavelengths for p - or s -polarized beams, respectively.

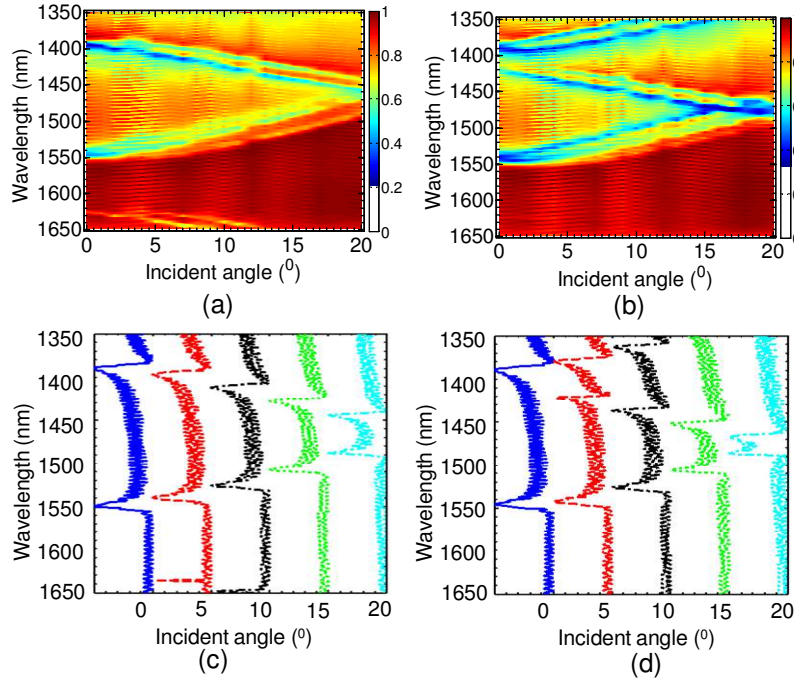


Fig. 8. Measured transmission intensity contour plots under different polarizations (a) Γ - M direction with p -polarization light (b) Γ - M direction with s -polarization light; (c) Simulated transmission spectra with p -polarizations; and (d) (c) Simulated transmission spectra with s -polarizations.

Following a similar procedure, the measured transmission intensity contour for the hybrid polarization with ($\Psi = 45^\circ$) is shown in Fig. 9(a), along with the simulated transmission spectra shown in Fig. 9(b). The two sets of results agree very well with each other. The specific modal properties can be further explained with the dispersion plot, as shown in Fig. 9(c), for the wave vector along the Γ - M direction, which corresponds to the Region II shown

in Fig. 2(b). Again, different polarization modes can be identified, by correlating the measured transmission spectra with the simulated dispersion curves.

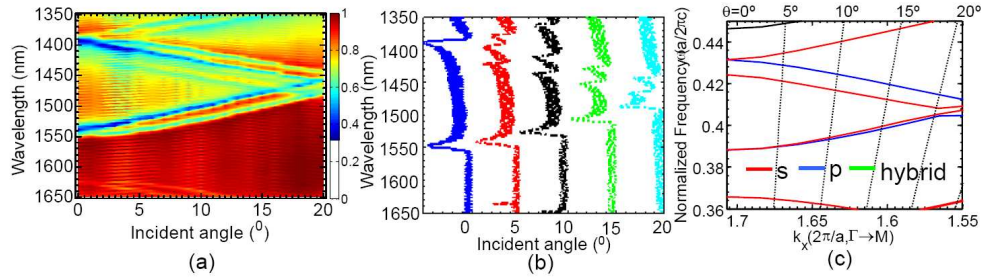


Fig. 9. (a) Measured transmission intensity contour plots for incident beam lies at 45 degree off x - z plane (Γ - M direction) with hybrid polarization ($\psi = 45^\circ$). (b) Simulated transmission spectra for different incident angles with the same incident beam orientation and polarization shown in (a). (c) Dispersion plot along Γ - M direction shown both p - and s -polarization states.

3.4. Discussions about the filter transmission contrast ratio

One of the key parameters in the filter design is the filter transmission contrast ratio, which is defined as the ratio of transmission intensities at pass and block (resonance dip) bands. We summarized both simulation and experimental results in Fig. 10, based on the data presented in Fig. 5, Fig. 7, Fig. 8, and Fig. 9 before. The simulated transmission contrast ratio varies from 14dB to 38dB, for both s - and p -polarizations. However, for the hybrid or unpolarized beams, the simulated transmission contrast ratio is substantially reduced to 4-20dB, despite an excellent agreement was observed in the spectral location and spectral shift behaviors shown earlier. These results suggest that these filters are better suited for polarized incident beam applications, with high transmission contrast ratios. It can be designed for unpolarized or hybrid-polarized beams, provided the lower transmission contrast ratio is acceptable.

Also notice that the measured contrast ratio is constantly much smaller than the simulated one. Such performance degradation could be contributed both to the device imperfections in the structures fabricated, as well as to some test limitations/variations associated with the experimental setup. Notice we used here a broadband white light source (QTH lamp) and a focus objective lens to obtain the desired small beam size for testing. In this case, the focused beam size on the device area is relatively large, $\sim 150 \mu\text{m}$ in diameter (i.e. ~ 150 periods of air hole area of filters) for device pattern area of $1000 \mu\text{m}$ or above. It is anticipated that the real device size will be in the order of 10 - $100 \mu\text{m}$. With a wideband tunable laser source, a much smaller beam size (e.g. 10 - $50 \mu\text{m}$) can be obtained, which can measure the actual cavity Q for a device area of 10 - 100 periods of air holes. A better agreement between the measurement and the simulation may be obtained due to potentially smaller lattice variations. The measured transmission contrast ratio can approach the simulated one. Further work is undertaken to address these concerns for real device applications.

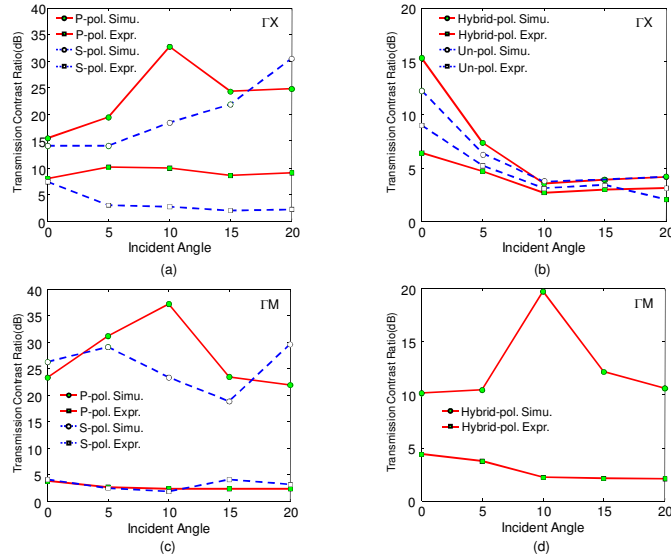


Fig. 10. Comparison of the simulated (Simu.) and experimental (Expr.) transmission contrast ratios for the dominant resonant modes for beam along: (a) ΓX direction for p- and s-polarizations (Fig. 5); (b) ΓX direction for hybrid-polarization and un-polarized beams (Fig. 7); (c) ΓM direction for p- and s-polarizations (Fig. 8); and (d) ΓM direction for hybrid-polarizations (Fig. 9).

4. Conclusion

In conclusion, the angular and polarization dependent properties were reported for Fano resonances with transferred Si nanomembranes on glass substrates. For surface-normal incident beam, there is no angle/polarization dependence on the spectral locations of Fano resonances based on transmission spectra. On the other hand, when the incident beam is not surface-normal, different Fano resonance modes appear to have drastically different angular- and polarization- dependent transmission properties. The spectra shift is largely dependent on the polarization states of incident beam, the direction of the incident beam and, the phase matching conditions. It is feasible to have different spectral shifting characteristics, either red- or blue-shifts, at various shift rates ranging 0.5 to 5 nm/degree. The measured spectral shift results agree very well with both the simulated spectral shift results, as well as with the polarization modal properties, based on the simulated dispersion plot. These findings will provide important aid to the design of Fano filters based on transferred SiNMs on glass substrates, for desired angular- and polarization- and spectral transmission properties. The results show that Fano resonance based silicon nanomembrane devices can be ultra compact and flexible, for application such as modulators, directional photodetectors, sensors, beam splitters, as well as micro-reflectors. Notice that typically a lateral lattice period of $15a$ is sufficient to achieve compact, yet, high performance photonic devices [25]. With further process optimization, these transferred nanomembranes can find wide and practical applications in various electronic and photonic device and integration system applications.

Acknowledgments

The authors appreciate the support from AFOSR Nano (FA9550-06-1-0482 and FA9550-06-1-0487), and AFOSR MURI program (FA9550-08-1-0337). The authors also thank the fabrication support from the University of Texas at Arlington NanoFAB Center and the University of Texas Austin MRC center, part of NSF NNIN sites.